Cell. Mol. Life Sci. 63 (2006) 1106–1124
1420-682X/06/101106-19
DOI 10.1007/s00018-005-5522-4

Cellular and Molecular Life Sciences

Review

Magnetic resonance and the human brain: anatomy, function and metabolism

I.-F. Talos[a], A. Z. Mian[b], K. H. Zou[a, c, *], L. Hsu[a], D. Goldberg-Zimring[a], S. Haker[a], J. G. Bhagwat[a] and R. V. Mulkern[a, d]

[a] Department of Radiology, Brigham and Women's Hospital, Harvard Medical School, 75 Francis Street, Boston, Massachusetts 02115 (USA), Fax: +1 617 264 6887, e-mail: zou@bwh.harvard.edu
[b] Department of Radiology, Boston University, Boston, Massachusetts (USA)
[c] Department of Health Care Policy, Harvard Medical School, Boston, Massachusetts (USA)
[d] Department of Radiology, Children's Hospital, Harvard Medical School, Boston, Massachusetts (USA)

Received 1 November 2005; received after revision 11 January 2006; accepted 25 January 2006
Online First 29 March 2006

Abstract. The introduction and development, over the last three decades, of magnetic resonance (MR) imaging and MR spectroscopy technology for *in vivo* studies of the human brain represents a truly remarkable achievement, with enormous scientific and clinical ramifications. These effectively non-invasive techniques allow for studies of the anatomy, the function and the metabolism of the living human brain. They have allowed for new understandings of how the healthy brain works and have provided insights into the mechanisms underlying multiple disease processes which affect the brain. Different MR techniques have been developed for studying anatomy, function and metabolism. The primary focus of this review is to describe these different methodologies and to briefly review how they are being employed to more fully appreciate the intricacies associated with the organ, which most distinctly differentiates the human species from the other animal forms on earth.

Keywords. Magnetic resonance imaging (MRI), magnetic resonance spectroscopy (MRS), brain, anatomy, function, metabolism.

Introduction

Studies of the brain with magnetic resonance (MR) imaging (MRI) and MR spectroscopy (MRS) methods have become commonplace and play increasingly important roles in both modern neuroscience and radiological practice. For example, as of 1994, Riederer [1] estimated that there had been some 40,000 functional MRI (fMRI) research studies alone. Similarly, the installation base of MRI scanners for clinical examinations throughout the world has grown steadily since the early 1980s and MRI now represents a very lucrative sector of the medical industrial complex. It is indeed amazing how such a relatively complex physical phenomenon like MR, discovered some 65 years ago and first appreciated by only a handful of physicists, has become such a commonplace and important part of modern science and medicine.

The transformation of MR from obscure roots to widespread practicality is a tribute to the rich and varied information contained in the MR signal from different materials. In neuroscience and radiological applications, the MR signal of primary interest arises from the protons of the hydrogen atoms of water molecules and lipids. The ability to spatially encode the MR tissue water signal so that images can be made enables detailed studies of brain anatomy and brain function. A vast amount of metabolic information can also be gleaned from MR signals arising from molecules other than water. Though much weaker

* Corresponding author.

than the water signal due to lower concentrations, many MR signals from brain metabolites are accessible with modern scanners.

Here we will review the primary methods employed when applying MR to studies of the living human brain. Specifically, the more generic MRI methods used to acquire data for anatomic or morphological studies, including tissue segmentation methods for quantitative structural measurement are described. This is followed by a discussion of the MR methods used for functional studies of the brain including the so-called BOLD effect and methods designed to measure tissue perfusion. Finally, the spectroscopic methods for extracting information on biochemical processes and brain metabolism are presented along with topical applications. The general approach is to describe the MRI and MRS methods and the types of information available from them that are currently contributing to our evolving understanding of the living human brain.

Morphology

Conventional imaging

There are several types of conventional MRI scans used to obtain morphological information about the brain. These scans form the basis of most clinical brain examinations but also provide data from which quantitative image analyses can be performed to obtain, for example, volumes of structures of interest. The physical principles of MR image formation are beyond the scope of discussion but can be found in several texts and articles [2–6]. What is critical to understand is that MR images of the same anatomy are routinely made but with different tissue contrast. The tissue contrast observed in any given image is the result of an interplay between the intrinsic tissue properties and the specific pulse sequence and pulse sequence parameters employed to generate the image. The intrinsic tissue properties primarily responsible for tissue contrast are the proton density, PD, and the longitudinal and transverse relaxation times, T1 and T2, respectively. The most common images acquired are T1- and T2-weighted images in which the tissue contrast is weighed to reflect differences in the T1 and T2 relaxation times among the different tissues. Also of interest are the PD images, in which the tissue contrast primarily reflects differences in tissue water content, and fluid attenuated inversion recovery (FLAIR) images which are generally T2-weighted images but without the signal from cerebral spinal fluid (CSF) that is normally very bright on T2-weighted images. Typical images of an axial slice at the level of the basal ganglia acquired at 1.5 T with each of these different tissue contrast weightings are provided in Figure 1. These images were acquired at the common field strength of 1.5 T using spin-echo or so-called fast spin echo approaches [6–11]. Prior to discussing the actual tissue contrast in these images, we review the basic formulae used to account for the signal intensities among different tissues as acquired with basic spin echo type sequences. The signal intensity S, for a given voxel of tissue in the spin echo sequence is given by

$$S = k\,(PD)\,[1 - \exp\,(-\,TR/T1)]\,\exp\,(-\,TE/T2) \qquad \text{(Eq. 1)}$$

In this expression, k is a relatively unimportant constant of proportionality which depends on factors such as the voxel size, receiver gain and receiver coil sensitivity. The repetition time TR is how long one waits in between exciting the volume being imaged, as multiple signals are required for image formation [2–6], and generally ranges from 300 to 6000 ms depending on the degree of T1-weighting one wishes to impart. The echo time, TE, is how long one waits after the excitation to the center of the echo signal readout and determines the extent of T2-weighting. For fast spin echo sequences, an effective echo time or ETE is used in which the T2-weighting is determined by the time after excitation at which the lowest phase-encoding gradients are applied [6, 8–11]. Typical echo times for T2-weighted imaging of the brain are of the order of 60–120 ms. Table 1 summarizes the approximate T1 and T2 relaxation times for gray matter, white matter, CSF and scalp lipids at 1.5 T [12, 13]. In general, tissue T1s increase with field strength while T2, dogmat-

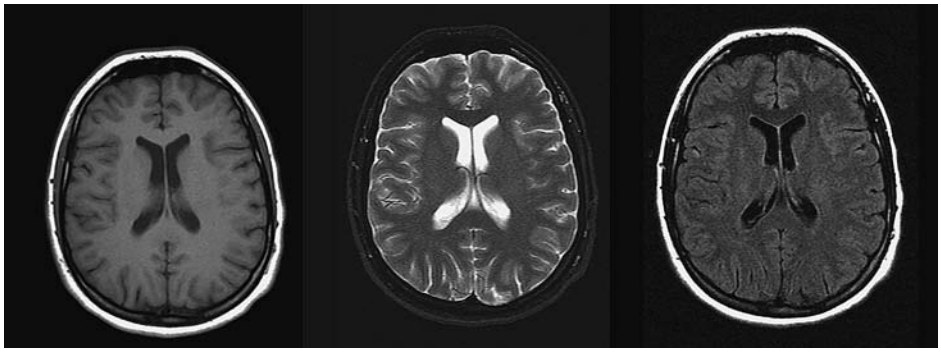

Figure 1. Axial T1-weighted (left), T2-weighted (middle) and FLAIR images (right) at the level of the basal ganglia in a healthy adult.

Table 1. Typical T1 and T2 values for the normal tissues found when imaging the brain at 1.5 T.

Tissue	Gray matter	White matter	CSF	Scalp lipid
T1 (ms)	700–900	550–750	2000–5000	200–300
T2 (ms)	80–100	60– 80	1000–2000	40–150[1]

[1] The large range of lipid T2s reported is due to J-coupling effects which cause the actual value of T2 to depend on precisely how it is measured, with longer T2s recovered from fast spin echo vs spin echo sequences.

ically stated to be field independent, does show some decrease with field strength [14–17]. Thus, adjustments of spin echo pulse sequence parameters TR and TE (or ETE) are in order when, for example, brain protocols are transferred from 1.5 T to ever more popular 3 T platforms (Table 1).

Equation 1 shows how changes in TR and TE bring about different signals from different tissues and demonstrates how one can select them to optimize signal intensity differences between tissues. For example, consider a T2-weighted imaging protocol in which the TR is long enough (greater than say 4 s) to make T1 contributions relatively negligible. Given a white matter T2 of 60 ms and a gray matter T2 of 80 ms, one can readily show from Eq. 1 that a TE of approximately 70 ms will maximize the contrast between gray and white matter. FLAIR imaging requires that an additional 180 inversion pulse be placed some 1.5 s prior to the excitation pulse. This delay, called the inversion time, TI, is set so that the longitudinal magnetization from CSF, a long-T1 'tissue,' is close to 0 when the excitation pulse arrives, effectively nulling CSF signal even when T2-weighting is dialed in with the TR and TE. For inversion recovery imaging, Eq. 1 is multiplied by the additional factor $[1 - \exp(-TR/T1)]$ and, aside from FLAIR imaging, shorter inversion times of the order of 150 ms at 1.5 T are also used to null fat signal which is useful for imaging around the orbits [18].

In addition to the different tissue contrast weightings available from routine MRI, the spatial resolution and imaging formats typically employed should be considered. For routine applications, signals are acquired from 'slices' of tissue that are between 2 and 10 mm thick. The actual image of each slice is reconstructed in a two-dimensional (2D) format once enough signals from a given slice are acquired. The in-plane spatial resolution is generally higher than the 'through plane' slice thickness and is typically of the order of 1×1 mm^2. Most 2D acquisitions utilize no gap or only a small gap between the slices. However, when multi-slice 2D image data sets acquired in one plane are reformatted for viewing from another plane or vantage point, the anisotropic spatial resolution can result in considerable image quality degradation. This is demonstrated in Figure 2 in which a coronal image reformatted from a set of 3-mm-thick axial slices is shown. Thus, for improved visualization of anatomy from multiple angles, more isotropic acquisitions are performed using so-called three-dimensional (3D) acquisitions. The most common 3D acquisitions are performed using so-called spoiled gradient echo (SPGR) sequences in which signals from the 3D volume of the brain are acquired every 10–30 ms. From such acquisitions, generally lasting some 5–15 min depending on the particular sequence parameters, fairly isotropic spatial sampling of the order of 1×1×1 mm^3 becomes available. Figure 3 demonstrates how images from 3D acquisitions, generally acquired with a T1-weighted tissue contrast, makes reformatting from one plane to another much more feasible and also allows for more reliable estimates of the shapes and sizes of different structures. When considering tissue contrast for the so-called SPGR sequences commonly used for 3D

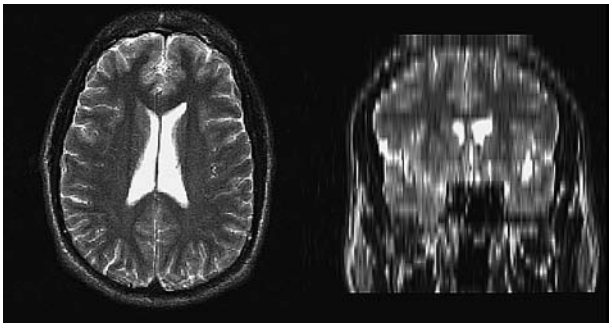

Figure 2. Axial T2-spin echo at the level of corona radiata (left) and a reformatted coronal slice from the original T2 data set (right). Due to the space between slices in the original acquisition, the quality of the reformatted coronal image is significantly lower.

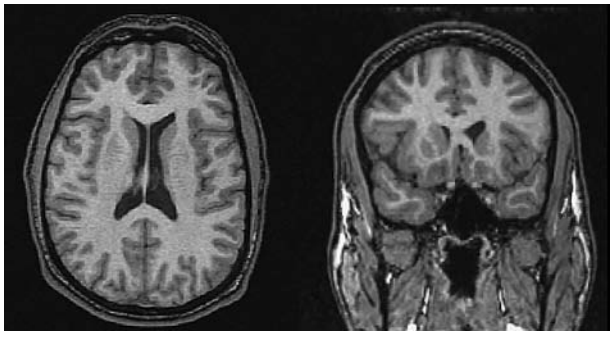

Figure 3. Axial 3D SPGR (left) and a reformatted coronal slice from the original SPGR (right). There is no significant quality difference between the original and reformatted image, since the data were acquired in a contiguous manner, without gaps between slices.

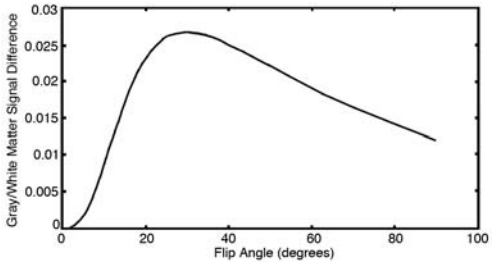

Figure 4. Signal difference between white and gray matter as a function of flip angle for a fixed TR.

brain studies, an additional pulse sequence parameter, the flip angle α, of the excitation plays a role:

$$S = \{k\,(PD)[1 - \exp(-TR/T1)]\exp(-TE/T2)\sin\alpha\}/ [1 - \cos\alpha\exp(-TR/T1)] \quad \text{(Eq. 2)}$$

As with the spin echo sequences, parameters can be readily optimized to maximize contrast between for example gray and white matter using Eq. 2. The plot in Figure 4 shows the simulated signal intensity difference between gray and white matter with assumed T1 values of 850 and 650 ms as a function of the flip angle when the TR and TE were fixed at 35 and 5 ms, respectively, with T2 effects considered negligible for this short TE. Maximum contrast is achieved when a flip angle around 30° is selected, suggesting its use for this application.

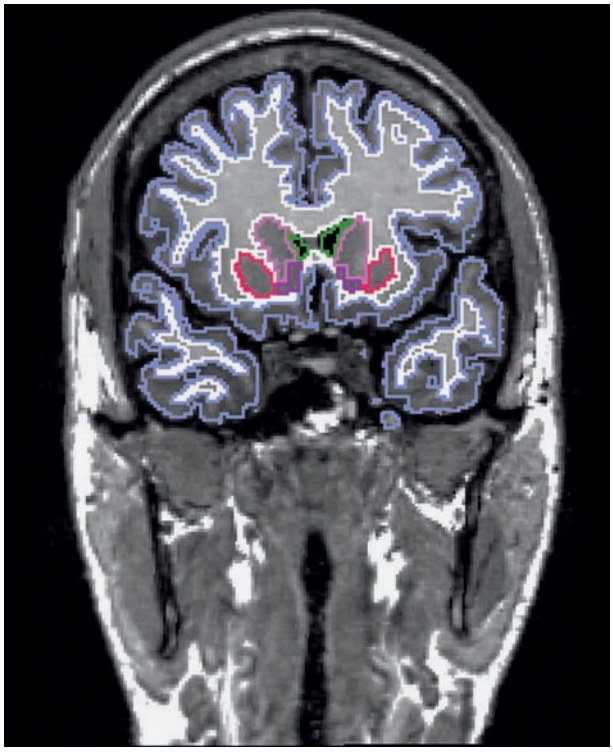

Figure 5. Segmentation of cortical gray matter (blue), hemispheric white matter (gray), caudate nucleus (pink), putamen (red) and lateral ventricles (green) on a coronal MPRAGE slice.

It is important to emphasize that routine MRI sequences are highly sensitive to intracranial pathologic processes. However, their specificity is limited. Intracranial lesions of diverse etiologies often show up as hyperintensities on T2-weighted MRI, e.g. brain tumors, inflammatory and demyelinating processes, post-traumatic lesions. On the same note, any process leading to a disruption of the blood-brain barrier, regardless of its etiology, will invariably lead to contrast enhancement on T1-weighted MRI. Examples include malignant primary brain tumors, metastatic tumors, brain abscesses and ischemic and post-traumatic lesions. Therefore, the capabilities of conventional MRI for accurately determining the extent of infiltrative intracranial processes, such as malignant primary brain tumors, are limited, since only the most aggressive tumor areas, completely lacking a blood-brain barrier, can be reliably outlined with contrast agents. On the other hand, treatment effects such as 'radiation necrosis' are often indistinguishable from actively growing tumor tissue based on their appearance on conventional MRI.

Conventional MR acquisitions serve as a basis for various morphometric and volumetric studies, based on segmentation and 3D reconstruction algorithms (Figure 5).

Diffusion imaging

Apart from the morphological information obtained from conventional MRI scans, a realm of structural imaging has emerged which employs the preferred directional diffusive motions of water molecules within the brain, principally white matter fiber tracts. The physical principles of diffusion imaging have been extensively described in the literature [1, 19, 20], so here we simply provide a brief overview of the basic principles and range of current diffusion imaging techniques, from simple diffusion weighting to diffusion tensor tractography.

Diffusion imaging quite generally refers to sensitizing MR images to the molecular motion of the water molecules. Sensitizing MR signals to molecular diffusion was introduced in the mid-1960s by Tanner and Stejskal who placed a pair of balanced magnetic field gradients about the 180 refocusing pulse of a spin echo sequence [21]. Varying the gradient strength, g, gradient pulse durations, δ, and separation between the leading edges of the gradient pulses, Δ, leads to different levels of spin echo signal attenuation from the diffusive motions of the water molecules quantitatively represented by the diffusion coefficient, D. The diffusion sensitivity is thus expressed by the b factor given by:

$$b = (g\gamma\delta)^2(\Delta - \delta/3) \quad \text{(Eq. 3)}$$

where γ is the proton gyromagnetic ratio ($2\pi\times4258$ Hz/Gauss) and the spin echo signal is attenuated by the fac-

tor exp(– bD). The most straightforward measurement of the molecular diffusion coefficient D is readily performed by acquiring two signals, S_o and S_1, with different b factors, b_o and b_1. The diffusion coefficient, D, is then estimated from the ratio of the two signal intensities via:

$$D = (b_1 - b_o)^{-1} \ln (S_o/S_1) \quad \text{(Eq. 4)}$$

where b_1 is the larger of the two b factors. Typically, b_o is very small, of the order of 5 s/mm^2, while b_1 values are generally in the 750–1000 s/mm^2 range. Tissue diffusion coefficients are conveniently expressed in units of μm^2/ms and typically range from 0.1 to 3 μm^2/ms.

Modern MRI technology has proven highly adaptable to diffusion imaging with the Tanner-Stejskal balanced gradient approach, since spin echo imaging sequences which use magnetic field gradients for signal localization are commonplace imaging strategies. Le Bihan et al. [22] were the first to incorporate the classic Tanner-Setjskal pulsed gradient pair about the refocusing pulse within spin echo imaging sequences and generated the first diffusion-weighted images of the human brain. Though the basic spin echo imaging approach is still viable, single-shot echo planar imaging (EPI) readouts are now generally employed to hasten the imaging process and reduce motion artifact [23].

It was soon recognized that water diffusion in tissue was subject to many more motion pathways than, for example, water molecules within a cup of tea. Restrictions to diffusion in the form of myelin sheaths, cell membranes and/or intracellular organelles and the complex, tortuous pathways associated with capillary beds significantly increase the complexity of the diffusion process within tissue. Thus the simple exponential decay with increasing b factor and the independence of the measured diffusion coefficient on the so-called 'diffusion time,' $\Delta - \delta/3$, within the b factor definition, are generally not features of tissue water diffusion. Because of these complications, the term 'apparent diffusion coefficient' or ADC has been extensively used to describe tissue water diffusion. The word 'apparent' could, however, just as well be applied to other tissue contrast parameters associated with MRI, like the transverse relaxation time T2, and so we refrain from using the term ADC. It must be recalled, though, that measurements of the tissue water diffusion coefficient D reflect many complicated motions, so that the details of the acquisition pulse sequence will significantly influence the measured value of D. The most obvious example of this phenomenon is the sensitivity of D to the direction of the diffusion sensitization gradients [24–32], which we will now discuss.

Myelinated fiber tracts within white matter of the mature brain and the extracellular space separating them offer a preferred direction for water molecules to travel, similar to what water molecules might experience in the fibers of a stalk of celery. As a consequence, the value of D measured with the diffusion sensitization gradients aligned with the fibers is found to be larger than the value of D measured with the gradients applied perpendicular to the fibers [33, 34]. To obtain a measure of D which is 'rotationally invariant,' or independent of the particular diffusion sensitization direction employed, the concept of a scalar value for D, which is appropriate for isotropic diffusion in simple liquids, must be abandoned for the more general diffusion tensor characterization [35–38]. The diffusion tensor model utilizes a 3×3 symmetric matrix, the diffusion tensor, with six independent elements that must be evaluated by sampling a minimum of six non-collinear diffusion sensitization directions. The diffusion tensor is a mathematical object with specific properties, and a convenient conceptual representation of the tensor is that of an ellipse with three principal axes, generally a long axis and two shorter, perpendicular axes which may or may not be of equal length. The lengths and directions of the three axes are the eigenvalues and eigenvectors of the tensor, respectively, and are calculated by diagonalizing the 3×3 diffusion tensor matrix. They represent the primary, secondary and tertiary modes of diffusion within a given image voxel.

The simplest application of the diffusion tensor model involves measuring diffusion coefficients along three orthogonal directions, an approach which yields sufficient information to obtain the sum of the diagonal elements of the matrix, or the trace of the matrix. The trace is rotationally invariant, or independent of the three orthogonal directions used for its measurement, and thus provides a robust measure of a tissue-specific 'average' diffusion coefficient D_{ave} given by:

$$D_{ave} = (D_{xx} + D_{yy} + D_{zz})/3 \quad \text{(Eq. 5)}$$

where D_{xx}, D_{yy} and D_{zz} are the diagonal elements of the diffusion tensor. Using only three diffusion sensitization directions keeps diffusion acquisitions relatively short compared to full tensor acquisitions. Furthermore, they are generally sufficient for the primary clinical application of diffusion imaging which is the detection of acute ischemic stroke [39–41] (Fig. 6). The impaired function of the cell membrane Na-K-ATPase following ischemia, with consecutive intracellular accumulation of Na and water molecules (intracellular edema) is responsible for this effect.

For studying the integrity and depicting the directionality of white matter tracts, however, additional information from the full diffusion tensor is generally sought, requiring the use of least six diffusion sensitization directions and a baseline (b_o) acquisition. This approach requires more scan time but yields several rewards once all six diffusion tensor elements are estimated. The most commonly reported of these rewards is a rotationally invariant

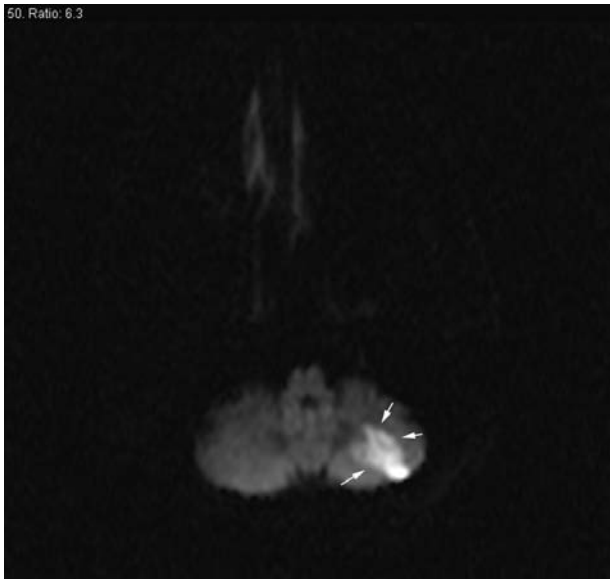

Figure 6. Diffusion-weighted MRI showing a hyperacute ischemic stroke in the left cerebellar hemisphere (arrows).

measure of the diffusion anisotropy, embodied by the so-called fractional anisotropy, FA, parameter given by:

$$FA = [(\lambda_1 - \lambda_2)^2 + (\lambda_2 - \lambda_3)^2 + (\lambda_1 - \lambda_3)^2]^{1/2} / [2(\lambda_1^2 + \lambda_2^2 + \lambda_3^2)]^{1/2} \quad \text{(Eq. 6)}$$

where λ_1, λ_2 and λ_3 are the eigenvalues of the diffusion tensor obtained using all six tensor elements including the off-diagonal elements D_{xy}, D_{xz} and D_{yz}. The FA value ranges from 0 to 1 and is a rotationally invariant measure of the how 'anisotropic' the diffusion of water molecules is within a given voxel. For example, if a water molecule is equally likely to wander off in any given direction, as in our hypothetical cup of tea, then the diffusion is said to be isotropic and FA is 0. If, on the other hand, the water molecule is forced to wander along only one direction, as in a severely restricted microtubule, then the diffusion is highly anisotropic and the FA approaches unity. Typical values for FA in mature white matter are in the 0.15–0.90 range and are generally thought to reflect, to some degree, the extent of myelination and the thickness of the axons, though even unmyelinated fibers provide enough restrictions to motion that anisotropic effects are observed [23, 25, 42, 43].

In addition to the FA, the directions of the three eigenvectors – primary, secondary and tertiary – are obtained for each voxel. These directions, especially that of the primary eigenvector, are often mapped with vectorial displays. More complex color displays and/or maps of the tensor ellipses, all of which reflect characteristics of the three eigenvectors and their rank order, have also been employed for visualizing diffusion tensor information [36, 44–46].

As diffusion tensor imaging (DTI) developed, an interest in proceeding beyond assessing the diffusion properties of individual voxels and towards generating information regarding inter-voxel relationships began to grow. Specifically, it became of interest to infer and display actual white matter fiber tracts coursing through large regions of the brain from diffusion tensor data. And thus the reckless daughter of DTI, diffusion tensor tractography (DTT), was born [26, 28, 29, 31, 47]. Several approaches for performing DTT have now been proposed and have begun to provide a powerful new tool for exploring brain connections. The basic idea behind DTT is to determine the most likely route by which a water molecule enters or exits a voxel, as based on the primary preferred direction of diffusion within a given voxel and its neighbors. Typically, algorithms begin by selecting a 'seed' voxel from which the fiber tracking begins. From each new voxel encountered, the process is repeated and the daughter (water molecule) wanders along the path specified at each step by the primary direction of water diffusion, which is the presumed overall direction of the white matter fiber tracts. Though simple in principle, DTT is computationally demanding in practice. Furthermore, choosing the reckless daughter's path is fraught with dangers associated with noise, vanishing anisotropies, and strange voxels in which distinct fiber tracts may cross. Despite this tracking, algorithms proceed from voxel to voxel and leave behind a colored trail outlining the fiber tract like pieces of spaghetti. Sprinkling the brain with different 'seed points' allows for multiple paths to be formed and results in whole-brain tractographic maps (Fig. 7).

Both mechanistic [28, 30] and probabilistic [29, 31, 32] approaches to DTT have been employed, though basic thresholds must be selected by the operator when computing the fiber tracts. One example of a typical threshold

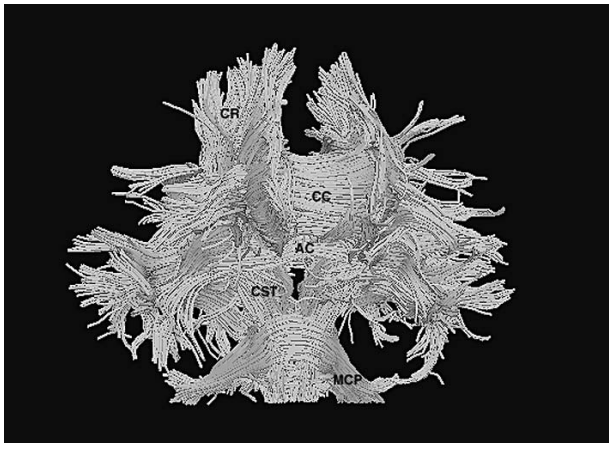

Figure 7. Diffusion tensor tractography in a healthy adult male. CR, corona radiata; CC, corpus callosum; AC, anterior commissure; CST, corticospinal tract; MCP, middle cerebellar peduncle.

parameter is the FA parameter discussed above. For example, if a voxel is found in which the FA value becomes quite low, then the tracking process has probably led to an area of gray matter or CSF and so should stop. Another threshold parameter often considered in deciding which way to proceed from a given voxel is the angle between the primary eigenvector within that voxel and the equivalent vector in the neighboring voxels. The inner product (IP) of two primary eigenvectors in voxels i and j:

$$IP = \boldsymbol{\lambda}_{ui} \times \boldsymbol{\lambda}_{uj} \quad \text{(Eq. 7)}$$

is proportional to $\cos\theta$, where θ is the angular difference between the vectors and thus is often used to help determine the path followed by the intrepid explorer. The FA and IP thresholds, or equivalent parameters depending on the precise DTT algorithm employed, are selected by the operator in an effort to insure that the tracking process will cease when minimal anisotropy or insufficient correlation of directions between neighboring voxels is observed, typically in gray matter or CSF regions. A good example of how FA and IP threshold values are optimized for axonal tracking in the brainstem is provided in the work of Stieltjes et al. [28] who used the fiber assignment by continual tracking (FACT) methodology. They found that intra- and inter-rater variability for identifying five major tracts in the brainstem were minimized when the FA and IP lower cutoff values were around 0.25 and 0.75, respectively [28]. Of course, the details of the acquisition such as the image plane (preferably selected orthogonal to major tracts of interest), the spatial resolution (isotropic vs anisotropic voxels) and the signal-to-noise ratio (SNR) all affect the performance of any given tracking algorithm. Even in its present form, however, DTT appears to fare well in qualitative comparisons of what is known regarding white matter fiber tract anatomy and it has become a fairly well accepted notion that DTT adequately identifies major fiber tracts and so allows for measurements of D_{ave} and FA along such tracts.

Aside from mapping connectivity between different cortical areas, DTI has several other important applications. Although myelin plays an important role in determining the anisotropic diffusion pattern in white matter, the diffusion anisotropy is diminished, but still present, in the absence of myelin. In cases of demyelinating lesions (e.g. multiple sclerosis), in the developing brain or during neural regeneration, the water diffusivity in the direction parallel to the axonal fibers ($\lambda\|$) remains widely unchanged, whereas the diffusivity in the direction perpendicular to the fibers ($\lambda\perp$) is increased. This is a useful feature for detecting areas of demyelination [48]. Another important DTI application is the detection of tumor-infiltrated white matter regions and characterization of tumor invasion of healthy brain parenchyma [49, 50]. It is important to emphasize that the information provided by DTI is purely morphologic in nature and this method cannot be employed for detecting functional activation within the cerebral white matter.

Function

Perfusion imaging

Two basic approaches for measuring aspects of blood perfusion in the human brain have been developed, one which utilizes exogenous contrast agents and one which does not. The former is currently more used and so is discussed first. The most common contrast agents in MRI are molecular chelates which contain the paramagnetic gadolinium ion Gd^{2+}, an example being the compound gadolinium-diethylene-triaminic acid (Gd-DTPA) [51]. The primary purpose of this contrast agent is to enhance signal from regions in central nervous system (CNS) tissue in which the blood brain barrier has been compromised by the presence of e.g. tumor, inflammation, ischemia or radiation necrosis, and this enhancement is most commonly appreciated on T1-weighted spin echo sequences. It has been known for some time, however, that such contrast agents also cause a transient decrease in the signal intensity of brain tissue on T2*-weighted images, as the agent courses through the brain vasculature in its ‘first pass’ and prior to its rapid distribution into the extracellular compartment throughout the body and ultimate excretion from the kidneys [40, 52–55]. This transient decrease in signal can be captured on T2*-weighted images of the brain acquired serially with temporal sampling rates of the order of 2 s and acquired for the first minute or so following bolus venous injection [52–54]. The T2*-weighting, high volume coverage and high temporal resolution of gradient echo EPI sequences are well-suited for tracking the signal dips throughout the brain. The strength and duration of the signal intensity ‘dips’ versus time after injection can be modeled to yield cerebral blood volume (CBF) maps by direct integration of the area of the dip. Using more sophisticated analyses which estimate the arterial input function from signal intensity versus time in a judiciously chosen artery such as the middle cerebral artery (MCA), CBF and actual perfusion estimates can be mapped throughout the brain [53, 55]. The acquisition techniques and post-processing schemes for converting multi-slice EPI data sets acquired over the course of the contrast administration are now fairly well-established and software for generating the various parameters available from such studies is provided by most manufacturers. The techniques have been employed to study blood volume and perfusion changes accompanying a variety of brain diseases such as tumors, stroke and hypoxic ischemic encephalopathy (HIE). Indeed in ischemic stroke, there is some indication that ar-

eas of prominent perfusion deficit but with only mildly restricted diffusion may represent salvageable tissue (so-called ischemic penumbra), so that combining perfusion and diffusion studies may be used for aggressive patient management [39–41].

A typical example of a perfusion study performed using the bolus-tracking approach is shown in Figure 8, in which a blood volume map of an axial slice is depicted. In this case, the red regions in gray matter are easily differentiated from the green regions of white matter in which the blood volume is lower.

Perfusion imaging of the brain may also be approached without the use of contrast agents by using so-called arterial spin-tagging (ASL) methods [56–59]. These essentially involve labeling blood spins via a magnetic 'tag' such as an inversion pulse, prior to their entry into the imaging volume. Comparison with images acquired with and without the arterial blood labeling serves to measure perfusion. For such studies, single-shot EPI provides a convenient imaging modality, particularly since the most common variations require at least two separate acquisitions. The use of spin-tagging techniques is very attractive due to the entirely non-invasive nature of the study and offers many intriguing possibilities, including perfusion-based fMRI studies. There are some limitations, however, including limited volume coverage efficiency and a complexity of modeling factors influencing perfusion estimates, such as, for example, the T1 values of blood and the delay times between tagging and imaging the slice(s) of interest. It is probably fair to state that the optimal methodology to be employed for ASL remains open and that clinical use of this non-contrast agent approach to perfusion imaging is not as well-established or routine as the contrast-agent-based approach.

fMRI and the BOLD effect

The term fMRI, might appear to be a very general term that might refer to the function of any organ in the body. The terminology 'fMRI,' however, has effectively been confiscated by practitioners specifically interested in brain function and, with over 40,000 'fMRI' papers in the literature since its inception some 15 years ago [1], there appears to be no turning back. A basic description of the methods and analyses of 'fMRI' is now provided with the general understanding that fMRI is a tool to determine those areas of our brains that 'activate' or 'function' as a consequence of the various mental and physical tasks which make up our lives.

Gray matter is rich in neuronal cell bodies and is the primary tissue associated with functional activation detectable by fMRI. Even before fMRI, it was well-known that specific regions of gray matter are associated with specific motor (e.g. finger tapping, foot movement), sensory (e.g. somatosensory, visual, auditory) and cognitive functions. Basically, when activated, these regions demonstrate a hemodynamic response that can be detected with suitable MRI methods. Many of the details responsible for the actual signal change accompanying the hemodynamic response are still under investigation [60], though there is general agreement that functional activation leads to an increase in arterial blood supply. As such, there is an increase of oxygenated blood rushing to the region of neuronal activation. This phenomenon is the essence of the so-called blood-oxygenation-level-dependent (BOLD) response. Basically, the increased levels of oxygenated blood means an increase of the oxyhemoglobin-to-deoxyhemoglobin ratio within the vessels of the activated area. Oxyhemoglobin is diamagnetic and deoxyhemoglobin is paramagnetic so that as the ratio of oxy- to deoxyhemoglobin changes, there is a magnetic

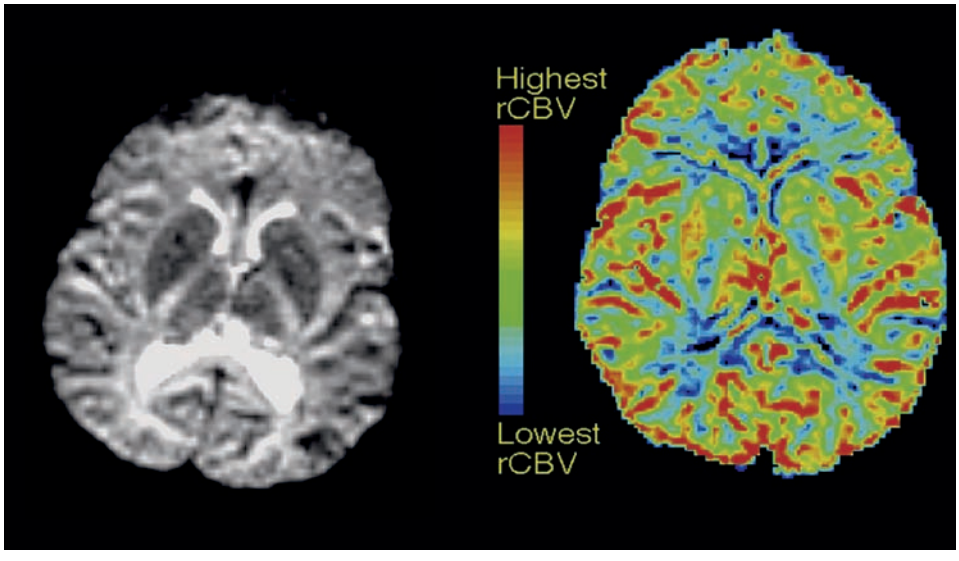

Figure 8. Perfusion study performed using the bolus-tracking approach, source image (left), blood volume map (right).

susceptibility change within the vessels of the activated area towards that of the magnetic susceptibility of the brain parenchyma. The resultant decrease in the magnetic susceptibility difference between vessels and parenchyma leads to a reduction in the microscopic magnetic field gradients surrounding the vessels. Using sequences in which the signal intensity is sensitive to microscopic field gradients, like EPI gradient echo sequences, this small effect can be detected as a reduction in the spin dephasing in the activated regions. In MR terminology, the reduced dephasing is described as an increase in the transverse relaxation time T2* = 1/R2*, where R2* is the transverse relaxation rate in s^{-1}. With a reduction of R2* by a small increment δR2*, the resultant T2* weighting of a gradient-echo-based image acquired with an echo time TE in the activated state is exp(–TE (R2* – δR2*), while the weighting for the unactivated state is exp(–TER2*). The difference between activated versus 'unactivated' state signals, ΔS, may be calculated to first order in TEδR2* as

$$\Delta S = [p(1 - \exp(-TR/T1))]\ TE\delta R2^* \exp(-TER2^*) \quad \text{(Eq. 8)}$$

Here, the term in brackets contains the standard spin density (p) and longitudinal relaxation time (T1) dependence, with TR being the repetition time. Most practitioners assume that changes in these two parameters are negligible between activated and unactivated states with the T2* dependence predominating gradient echo EPI scans. It is readily shown that the function described by Eq. 8 has a maximum at TE = 1/R2* = T2*. Thus it is common practice to employ gradient echo EPI sequences with TE values set between 45 and 75 ms for fMRI studies, as this is the approximate range of T2* values for brain parenchyma [61, 62].

Most fMRI studies utilize the signal change embodied by Eq. 8 to locate those regions of the brain that experience the hemodynamic response due to 'activation' or the BOLD response. The most common fMRI acquisition procedure is to scan the brain quickly with gradient echo EPI sequences, acquiring for example, 20 slices every 2.5 s. This is repeated for several minutes while, say, 30-s periods of activity (e.g. visual stimuli, finger tapping) are followed by 30-s periods of non-activity, and so on. The entire fMRI data sets are then analyzed for statistical differences between the 'on' and 'off' states using any number of software packages now available, such as the statistical parameter mapping (SPM99) package (http://www.fil.ion.ucl.ac.uk/spm/spm99.html) which is based on the linear model of Friston et al. [63]. The 'on-off' strategy, or 'blocked-task paradigm,' for stimuli presentation is by far the most commonly used. Figure 9 shows the typical motor activation of the hand area obtained during a simple finger-tapping task in a healthy subject. There

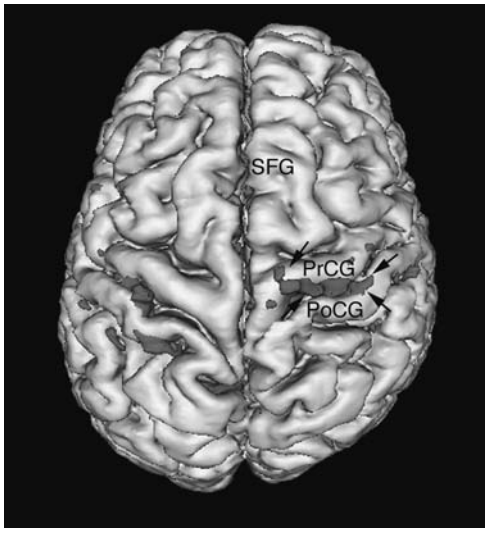

Figure 9. Motor activation (dark gray, arrows) during a simple left-finger-tapping task in a healthy subject. The 3D model of the brain was generated from a volumetric SPGR scan obtained during the same session as the fMRI scan. The functional and anatomic scans were rigidly registered. Note that there is also some degree of activation on the contralateral side. SFG, superior frontal gyrus; PrCG, precentral gyrus; PoCG, postcentral gyrus.

are, however, other strategies for stimuli presentation, such as 'event-related' responses [64, 65] which may be more appropriate for some types of cognitive tasks. In general, the mode of stimuli presentation is an important consideration when designing fMRI studies to address specific hypotheses.

The basic fMRI experiment just described was elucidated many years ago by several groups [66–68]. The description should be supplemented considerably for a full appreciation of the technique and its limitations. Spatial-resolution limitations and the complexity of the BOLD signal itself often make unambiguous localization of the truly activated areas problematic. For example, signal changes from regions near veins which drain activated areas can distort and/or magnify the size and shape of the activated regions. Furthermore, there has been some work suggesting that the spin density, p, may also be affected in regions near the BOLD activated regions, though work in this area is sparse [69]. A complete description of such effects lies beyond the scope of the present review, but should be appreciated when performing fMRI studies and choosing appropriate acquisition strategies [70–72].

Metabolism

MRS offers a unique view into metabolic processes of the human brain. Signals from many brain metabolites, typically the smaller-molecular-weight metabolites with concentrations in the 1 to several millimolar range, can be detected and, to varying degrees, quantified [73–75]. This

allows the study of steady-state metabolic levels in healthy and diseased brain tissue *in vivo*. It must be stated at the outset, however, and with some irony, that MRS really plays a very small role in clinical MR examinations despite the fact that it preceded the development of MRI by some 40 years and continues to play a fundamental role in physics, chemistry and biochemistry. On a more positive note, we speculate that MRS is probably far from achieving its full potential in the clinical realm. Namely, as higher magnetic field strengths of 3 T and greater become more common, MRS of both protons and other nuclei, such as phosphorous (^{31}P), carbon (^{13}C) and sodium (^{23}Na), will probably be more widely tested and adopted for specific clinical and/or research applications. Here, we briefly review the physics of MRS and the current methods used to perform MRS clinically. Then we discuss the information content and the typical clinical and research applications of proton MRS [76] as well as the potential utility of exploring signals from other, less accessible, 'MR-visible' nuclei.

MRS physics and methods

It is useful to begin a discussion of the physics of MRS with the concept of a 'bare proton,' that is a proton without any accompanying electron. The 'bare proton' will resonate in a magnetic field at the Larmor frequency due to the interaction of its magnetic moment with the applied magnetic field. As soon as one puts some 'clothes' on the proton by, for example, adding an electron as in a hydrogen atom, the resonant frequency is observed to shift a little bit. This shift is due to the response of the electron to the applied magnetic field, which, in diamagnetic substances, results in a microscopic electrical current that tends to 'shield' the proton from the applied magnetic field. This shielding effect, arising from intra-molecular electronic currents, is the basis of the famous 'chemical shift' in which the actual resonant frequency of a proton depends on the specific electronic bonding arrangement in which it finds itself. First-principle calculations of chemical shifts are exceedingly complex and require detailed knowledge of the ground state electronic wave functions as well as all their excited states [77]. Of more relevance to MRS practitioners, however, is the fact that the chemical shifts provide specific fingerprints of molecules that have been extensively catalogued and used by chemists for many decades in identifying chemical products.

In addition to the chemical shift differences between protons, additional intra-molecular interactions can exist between protons in chemically distinct environments via electronic coupling, the so-called J-coupling interactions [77]. When present, these interactions cause simple 'singlet' lineshapes to become more spectrally complicated doublets, triplets, etc. In such cases, the actual lineshapes can be quite complex and depend on precisely how they are measured. With *in vivo* MRS studies of the brain, specific pulse sequences have evolved for extracting the MRS data and the timing parameters of such sequences have effects on the observed signals that must be considered when targeting specific molecular signals. So we turn to a discussion of the techniques for extracting MRS data in the human brain.

Approaches for extracting MRS information from the brain range from the simplest 'single-voxel' approach to technically more demanding multi-voxel spectroscopic imaging methods. In the single-voxel approach, three slice-selective RF pulses are employed to sequentially excite or refocus three orthogonal planes in such a manner that the signal following the preparation arises from the intersection of the three planes. The most common strategy is to use a double spin echo sequence with a 90° excitation pulse followed by two 180° refocussing pulses, as in the so-called point-resolved echo spectroscopy (PRESS) approach [78]. An alternative strategy is to use three 90°-slice-selective pulses to solicit a 'stimulated echo' from the intersection of the three planes as in the so-called stimulated echo acquisition method or STEAM [79]. In either case, the 'single voxel' defined by the intersection of the three slice-selective pulses is the volume from which the spectral information is being extracted. Usually, because of the low concentration of metabolites, signal averaging is employed even with single voxel sizes of the order of several cubic centimeters. Thus, for example, a single voxel acquisition using a 2-s TR and 64 signal averages requires approximately 2 min of scan time.

The single-voxel approach, though still in use, is obviously limited in volume coverage. As scanner software and hardware has improved, the so-called multi-voxel approaches have become more common. Basically, for multi-voxel acquisitions, the single-voxel approach is simply modified by increasing the size of the selected voxel and incorporating spatial phase-encoding gradients in one, two or even three dimensions. Slice-selective RF pulses are still used to excite the volume of interest and, prior to each spectroscopic readout, phase-encoding gradients are applied as in conventional MRI [80]. The primary drawback is long scan times, as one must collect as many signals as there are phase-encoding steps. Thus, for example, a 16×16 2D spatial matrix to cover a slice in the brain will require 256 signals, so that using a 2-s TR, the scan time becomes of the order of 9 min. For 3D acquisitions of a volume, 16×8×8 spatial encoding matrices can be used with a 1-s TR to sample multiple voxels throughout the brain in approximately 17 min. Methods to decrease such long spectroscopic scan times do exist and include the use of echo planar spectroscopic imaging techniques [81] and parallel imaging approaches [82]. It should always be appreciated, however, that the SNR is, to first order, dependent on the square root of the overall

scan time. Thus, for each particular application, reducing scan time with a fast spectroscopic imaging technique must be weighed against the potential loss of SNR from the metabolites of interest. With this caveat in mind, we now turn to a discussion of the information content of proton MRS and non-proton MRS.

Proton MRS

An admirable review of the primary metabolites which contribute to proton spectra from the living human brain was provided by Miller some 14 years ago [73] and a more comprehensive review of both the major and minor metabolite signals was recently provided by Govindaraju et al. [74]. The major metabolites of interest are N-acetylaspartate (NAA), choline-containing compounds (Cho) and creatine (Cr) compounds including creatine and phosphocreatine (PCr). The biological relevance of these compounds has been fairly well studied, though the role of NAA in metabolic processes was largely motivated by its prominence within *in vivo* proton spectra of the living human brain [75]. Immunohistochemical studies have shown that NAA is predominantly located in neuronal cell bodies and their processes [83]. Consequently, this compound is generally considered to be a 'neuronal marker.' However, cell culture studies have been performed which report the presence of NAA also in non-neuronal cell types, such as oligodendrocytes [84, 85]. Furthermore, reversible NAA decreases in various pathologic processes such as multiple sclerosis and mitochondrial diseases have been reported. These findings suggest that a decrease in NAA may not always indicate neuronal loss [86]. Choline is the precursor of phosphatidyl choline, the main phospholipid in the cell membrane. An increase of Cho levels is associated with increased cell membrane turnover, as encountered in neoplastic processes. Creatine, a high-energy compound located in the mitochondria, serves as a marker for cellular energy metabolism.

The three major signals from NAA, Cho and Cr appear on the chemical shift scale at approximately 2.0, 3.2 and 3.0 parts per million (ppm), respectively. The water resonance on this ppm scale, which generally must be suppressed to be able to appreciate the much smaller signals from the metabolites, appears at approximately 4.7 ppm (note that we have dropped the traditional negative sign customarily accompanying these ppm assignments in the interest of simplicity, though the ppm axis will go backwards with higher numbers to the left along the x-axis ppm scale as a consequence of this historical relic). Resonances from lipids between 0.9–1.5 ppm and from the lactate molecule, the end product of anaerobic glycolysis [74], at approximately 1.3 ppm are often encountered in brain tissue as well, though they are largely absent in healthy brain parenchyma.

Because it is image guided, MRS is generally performed towards the end of individual MRI examinations when a number of scan planes and contrast options have been obtained to best visualize suspect pathology. Often this involves T1-weighted post-gadolinium injection images where suspicious regions are quite obvious. From any plane or any contrast option image, the operator graphically prescribes the voxel(s) for sampling. A pre-scan procedure shims over the volume to be sampled to reduce field inhomogeneity so that the linewidths of the individual resonances are within acceptable ranges, 5–12 Hz for example. Also, the pre-scan procedure adjusts the amplitudes of the chemical shift selective suppression (CHESS) water suppression pulses so that the normally overwhelming water resonance is reduced to acceptable levels.

Figure 10 shows a typical brain voxel and proton spectra acquired from the voxel at 1.5 T using the PRESS technique [76]. Two spectra are shown, one from a short-echo-time acquisition, TE = 31 ms, and one from a long-echo-time acquisition, TE = 135 ms. As with tissue contrast in imaging, one can manipulate the appearance and relative sizes of the spectral peaks by manipulating the echo times due to differences in the metabolite signal T2 values [87, 88]. A basic rule of thumb in this regard is that short-echo-time spectra contain many more signals from the heavier-molecular-weight metabolites than do the long-echo-time spectra. This may seem like an advantage, in that inherently more information is available. The drawback is that many of these resonances overlap and water suppression is usually less efficient for short TE values, making baseline estimations problematic. The longer-echo-time spectra tend to be much 'quieter' and easier to interpret, with flat baselines and only a few well-defined peaks, simplifying interpretation. In addition to TE manipulation, different repetition times (TR values) can be used to manipulate signal intensities, though generally TR values between 1 and 2 s are used to hasten mul-

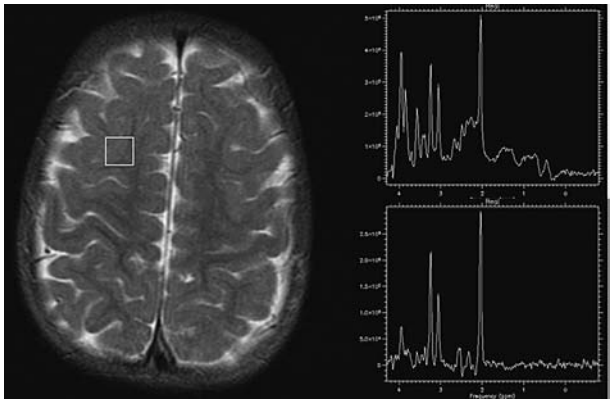

Figure 10. Axial brain scan showing the single voxel sampled for the TE = 31 and TE = 135 ms spectra shown top and bottom right, respectively.

tiple signal average acquisitions. As a result, metabolite signals, with typical T1 relaxation times of the order of 1 s, are partially saturated making T1 (and T2) corrections necessary when absolute quantification of metabolite signals is to be attempted [87]. Most clinical studies have relied on measuring the ratios of the metabolite signals such as NAA/Cr or Cho/Cr from long- or short-echo-time spectra in order to assess the value of proton MRS in differentiating healthy versus pathological brain tissue.

Figure 11 illustrates the typical differences in metabolite concentrations between neoplastic tissue and healthy brain parenchyma in a case of right perisylvian glioblastoma multiforme, as measured by single-voxel proton-MRS. Due to neuronal impairment and destruction, brain tumors show low concentrations of NAA, while the Cho levels are increased. This is mainly due to the high proliferation rate and increased cell membrane turnover [89]. Decreased Cr levels can also be observed in neoplastic tissue, likely due to an increase in the relative concentration of lipids. The Cho/NAA and Cho/Cr ratios tend to be higher in malignant gliomas, compared with their low-grade counterparts [90, 91].

More rigorous approaches in which estimates of absolute millimolar metabolite concentrations are made from the MR signals have also been established, however. One such approach is to use the unsuppressed water signal as a reference, assuming for example that water is 41.7 M in concentration [87]. The areas of the metabolite peaks can then be referenced with respect to the area under the unsuppressed water resonance and, with appropriate T1 and T2 corrections [87, 92], absolute metabolite measurements may be estimated. Alternatively, external references with known concentrations of a metabolite may be employed, though ultimately limitations in precision are set by receiver and transmit coil sensitivities. Thus, though it is possible to estimate absolute millimolar metabolite concentrations, the technical difficulties, complex post-processing and increased scan times required for relaxation time and/or coil sensitivity corrections have generally led to the use of metabolite ratios in clinical practice.

The size of the spectroscopic voxel sampled in Figure 10 is approximately $1.5\times1\times1$ cm^3, considerably larger than a typical $0.4\times0.1\times0.1$ cm^3 voxel volume used for MRI of

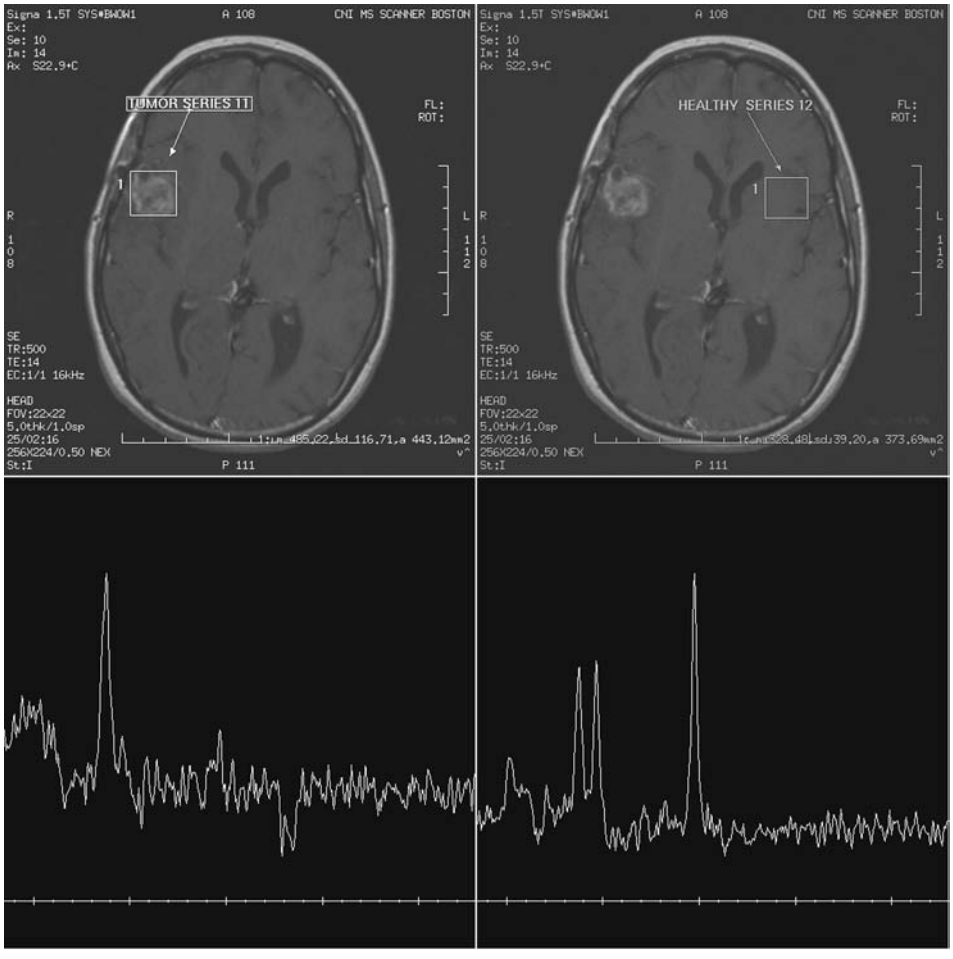

Figure 11. Proton-MRS in a case of right perisylvian glioblastoma multiforme. Left panel: spectra acquired from the tumor (increased Cho peak, decreased NAA and Cr peak). Right panel: normal spectra acquired from normal tissue on the contralateral side.

the brain. This is a consequence of the much smaller concentration of metabolites compared to water, a factor of 10,000 or more. Thus to attain sufficient SNR for metabolite detection in reasonable scan times, spatial resolution is reduced compared to MRI. Despite this drawback, MRS can be a valuable tool in helping to diagnose various brain disorders.

As discussed above, the NAA molecule and its signal are primarily associated with the intracellular space of neurons while the Cho resonance is thought to primarily arise from the tri-methyl proton groups of glycerophosphocholine (GPC) and phosphocholine (PC) with a minor contribution from free choline. Both creatine and phosphocreatine proton methyl groups contribute to the Cr resonance around 3 ppm, and high fields are necessary to differentiate these two molecules based on the small chemical shift difference between their respective methyl groups [73, 74]. Together, the three resonances of NAA, Cr and Cho provide a readily recognizable spectral pattern in normal brain tissue (Fig. 10) in which NAA is generally the largest of the three. There is of course an age-associated development of the relative strengths of the signals, as has now been documented from the fetus *in vivo* through old age, with Cho actually being the largest resonance in the spectrum during fetal development and perinatally [87, 88, 92–95]. There are also small but statistically significant regional differences in the relative strengths of the metabolite signals, including gray/white matter differences, as now documented in several adult brain studies [96–101]. Despite these complications, and those arising from studies using different acquisition methodologies (TRs TEs, etc.), there is now a generally recognized 'normal' spectral pattern for both short-echo-time and long-echo-time spectra. Departures from these normal brain spectral patterns are readily discerned by the eye for some pathologies like tumors, in which the Cho resonance generally dominates [102–105].

The increased Cho signal from tumor is generally useful when there is some question as to the nature of a non-contrast-agent-enhancing signal abnormality such as may be associated with a low-grade tumor, when identifying residual tumor in general and, in particular, when differentiating radiation-induced treatment changes from recurrent tumor [104, 105]. In such cases, the multi-voxel approach is preferred over single-voxel approaches since choosing where to place the single voxel from imaging characteristics alone may be difficult. In metastatic brain tumors, Sijens et al. [106] have shown that, in addition to an increased Cho presence in the spectral pattern, the presence of lipid and lactate signals can help differentiate early, intermediate- and late-stage disease. For other pathologies like multiple sclerosis [107, 108] or Alzheimer's disease [109–111], detecting subtle departures from the normal spectral pattern may require more sophisticated quantitative analyses that have become more widely available [112, 113]. Aside from clinical applications for diagnosis, basic studies of metabolic processes, including the absorption and removal from brain tissue of choline [114, 115] or even ethanol [116, 117] following oral ingestion, have been pursued with proton MRS and offer unique opportunities for studying biological aspects of how the brain and body process common chemicals.

As mentioned above, a lactate resonance is seen in many pathological conditions associated with anaerobic glycolysis. The spectral signature of lactate is quite specific due to the fact that it is a J-coupled, versus a singlet, resonance. Thus, for instance, the CH_3 lactate resonance appears as an inverted doublet in double spin echo spectra at echo times of 144 ms, a feature which can help distinguish it from the overlapping lipid signal of methylene (CH_2) protons. Lactate is of interest not only from the perspective of a pathology indicator but also as a functionally activated signal, though there remains considerable controversy about its detectability and value as a functional indicator in normal brain parenchyma [118–122].

Other coupled proton resonances from molecules such as glutamate, glutamine, myo-inositol, taurine and gamma-aminobutyric acid (GABA) are, in principle, accessible with *in vivo* brain MRS, offering opportunities to quantify these biologically active metabolites, particularly for research in neuroscience and psychiatry. Glutamate is an excitatory amino acid transmitter which can be neurotoxic at high concentrations, making it an important metabolite to quantify [123]. GABA is an important neurotransmitter playing a role in neurotransmission disorders, making it also of great interest to quantify *in vivo* [124, 125]. The specific chemical shifts and J-coupling patterns of such molecules have led to the development of advanced spectral editing techniques [126–131] and post-processing methods for spectral characterization, including the so-called LCModel approach [112, 132, 133]. With LCModel, a basis set of spectra from different metabolites, up to 18 or more for example, is used to fit *in vivo* spectra in order to quantify the complex signals and make estimates of the concentrations of metabolites contributing to these signals. The spectral editing techniques are used specifically to tease out only the signals from protons of selected molecules. The complicated procedures used are required since, in general, the multiple signals from these metabolites are not only small but tend to overlap each other in the 2–3 ppm range and are often swamped by more prominent singlet resonances like creatine. This is primarily why in the clinical environment, the signals from these more exotic resonances remain largely ignored, beyond an understanding that they contribute to noise-like peaks and baseline distortions around the 'feet' of the primary major metabolite signals from NAA, Cho and Cr. Nevertheless, as field strengths continue to increase and more sophisticated pulse sequences and post-processing strategies are brought to bear on the

problem, interest in the quantification of these less accessible metabolites will continue to grow and undoubtedly prove valuable in both research and clinical realms.

Non-proton MRS

The other nuclei which can be accessed with MR scanners, particularly at 3-T field strengths and higher, include ^{31}P, ^{13}C and ^{23}Na [134]. These nuclei have much lower sensitivities than water protons, meaning that they emit much lower portions of the administered RF radiation than protons, resulting in comparatively low SNRs. As such, large voxels from brain are generally sampled to obtain sufficient SNR in reasonable scan times when performing studies on humans. Despite this limitation, many studies have now been performed with these nuclei, each of which has an interesting story to tell regarding metabolic processes in the human brain.

^{31}P brain spectra provide distinct signals from the three phosphorus atoms in the ATP molecule, a resonance from inorganic phosphorus (Pi) and from PCr. Other signals from phosphomonesters and phosphodiesters are also present in the ^{31}P spectrum, but much of the focus has been on ATP, Pi and PCr signals as these play important roles in cerebral energetics. For example, the chemical reaction rates among the Pi, ATP and PCr molecules may be accessed with special saturation transfer pulse sequences in which the magnetization of one of these exchanging moieties is manipulated and its effect on the exchanging partner observed, as demonstrated during photic activation of the visual cortex. Steady-state differences in ATP and/or PCr concentrations and ratios between white and gray matter of the living human brain have been reported [135] and ^{31}P studies of numerous disorders including mitochondrial disorders [136], schizophrenia [137], diabetes [138], tumors [139], neonatal hypoxic ischemic injury [140] and migraines [141] have been performed. Of interest is that the ^{31}P spectrum can be used to both measure pH and to assess free magnesium levels in the brain, and these quantities are often reported along with metabolite concentrations or ratios.

Figure 12 is a representative 2D spectroscopic image acquisition using ^{31}P of a healthy adult brain. In this example, a 2-cm-thick slice was sampled using a selective 90 pulse followed by two phase-encoding steps so that the free induction decays were acquired starting within 2 ms of the excitation pulse. A 16×16 grid was sampled as shown in the image with a subsequent spectrum being provided from each 1.5×1.5×2 cm^3 voxel. A vial containing methylene diphosphanic acid located in the ^{31}P coil (not seen in the underlying proton image of the brain acquired with a proton coil) is responsible for the signal in voxels to the left but outside of the brain. A representative ^{31}P brain spectrum from the indicated white box towards the posterior of the brain as acquired with this 34-min acquisition using optimized k-space sampling and a 2-s TR is shown to the right and shows a prominent PCr peak at 0 ppm and the three ATP peaks at 3, 8 and 16 ppm.

Another nucleus of interest which can serve as marker for metabolic studies of the brain is ^{13}C. The ^{13}C nucleus is of very low abundance, however, compared to the much more abundant isotope ^{12}C which has no magnetic moment. Thus, although natural-abundance ^{13}C spectra from brain have been acquired [134, 142, 143], somewhat more intriguing studies have been performed using ^{13}C-enriched glucose infusion into the body [141, 144, 145]. As the primary substrate in normal adult human brain, the metabolism of glucose can be followed exquisitely as the

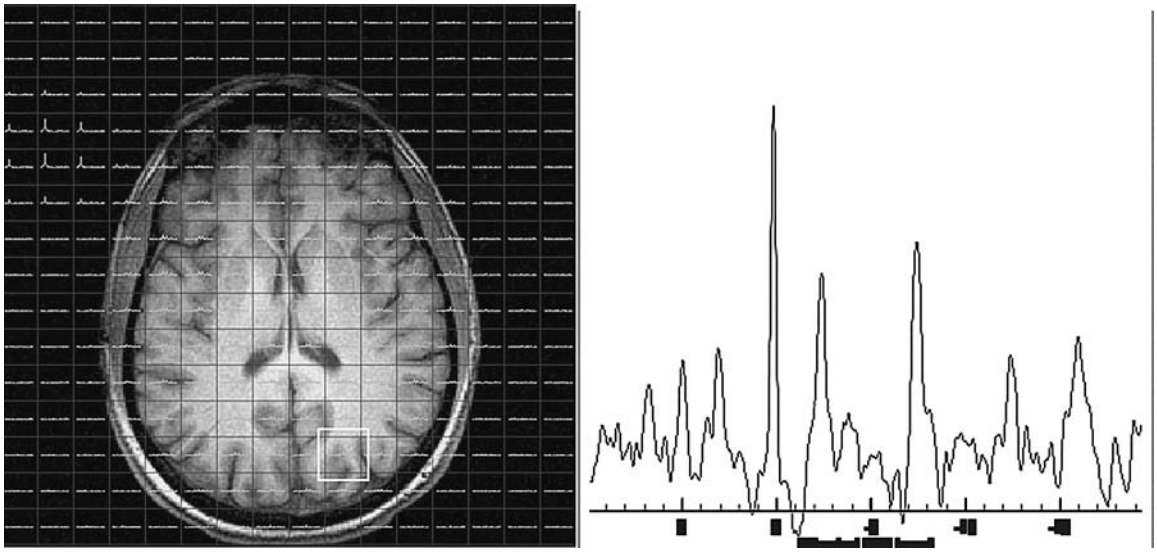

Figure 12. A 16×16 2D chemical shift image grid with corresponding ^{31}P spectra from each voxel overlaid on a proton image of the axial slice sampled. To the right is a ^{31}P spectrum from the white box indicated in the axial slice.

labeled ^{13}C on the glucose becomes labeled ^{13}C on other molecules along the two principal pathways of cerebral energy metabolism. For example, Bluml et al. [145] demonstrated increases in ^{13}C-enriched glutamate, glutamine and aspartate following infusion of ^{13}C-labeled glucose and also demonstrated the general safety of the procedure as applied to healthy adults, children and in patient populations. The authors propose that such infusion studies may prove useful for studying pathological changes in both adults and human newborns and yield valuable information regarding key steps in glycolysis and the tricarboxylic acid cycle. Primary impediments to such studies are the lack of multi-nuclear software on most clinical scanners as well as the expense of enriching chemicals with the rare ^{13}C isotope, though the feasibility and promise of such studies has been clearly demonstrated.

The last nucleus we would like to discuss is the sodium ^{23}Na nucleus. Compared to ^{31}P and even ^{13}C, ^{23}Na has not been as widely studied, partially due to a physical complication. Namely, ^{23}Na, unlike the other nuclei already mentioned, is not a spin 1/2 nucleus but rather a spin 3/2 nucleus and so possesses an electric quadrupole moment which considerably complicates its signal in biological material [146, 147]. Despite this feature, which makes for complicated and very rapid relaxation behavior, quite excellent imaging of the brain from the sodium nucleus has been accomplished over the last two decades [148–150]. Again, lack of widespread multi-nuclear hardware and relatively long scan times impede general use at this stage, though the intrinsically important role of sodium in maintaining cellular homoestasis clearly makes exploring the properties of its MR signal from the human brain a worthwhile endeavor.

Final remarks

Aspects of morphology, function and metabolism in the living human brain are all accessible with modern MR scanners. We have attempted to review the basic techniques and information available from MR, which are applicable to studying brain structure and function. This review has been, of necessity, non-comprehensive. Several interesting approaches to tissue contrast, including magnetization transfer techniques which are sensitive to the macromolecular content and its interaction with water molecules, as well as novel contrast agents in development for steady-state measurements of blood volume or more exotic 'molecular imaging,' have not been discussed. In addition, the entire area of image-processing techniques, in use and in development, to spatially register one type of information, high-resolution morphology images say, with lower-resolution fMRI maps of activation, have not been addressed. If there has been one common theme throughout the development of modern MR applied to the human brain it has been the interdisciplinary nature of the work involved. Contributions from physicists, physiologists, biologists, radiologists, neurologists, computer scientists, hardware engineers and chemists have all been critical for the rather amazing and continuing growth of our understanding of the living human brain through modern MR methods.

Acknowledgements. The authors are partially supported by the following grants, awarded by the National Institutes of Health, USA: R01-LM007861, P41-RR13218 and U41-RR019703. We would like to acknowledge Dr. S. Maier for the design and maintenance of the line scan diffusion imaging sequence used to acquire data for the diffusion tractography results and Dr. E. Jensen for the ^{31}P spectra of one of the authors (R. V. M.) acquired at McLean Hospital in Belmont, Massachusetts, in collaboration with Dr. D. Holtzman, and Dr. C.-F. Westin and the members of the Laboratory for Mathematics in Imaging at Brigham and Women's Hospital Boston for the design and implementation of the algorithm used for the diffusion tractography.

1 Riederer S. J. (2004) MR imaging: its development and the recent Nobel Prize. Radiology **231:** 628–631
2 Atlas S. W. (2000) Magnetic Resonance Imaging of the Brain and Spine, 3rd edn, pp. 33–100, Lippincott Williams & Willkins, Philadelphia
3 Hendee W. R. and Ritenour E. R. (2002) Medical Imaging Physics, 4th edn, pp. 355–401, Wiley-Liss, New York
4 Mulkern R. V. and Chung T. (2000) From signal to image: magnetic resonance imaging physics for cardiac magnetic resonance. Pediatr. Cardiol. **21:** 5–17
5 Twieg D. B. (1983) The k-trajectory formulation of the NMR imaging process with applications in analysis and synthesis of imaging methods. Med. Phys. **10:** 610–621
6 Mulkern R. V. (1992) In-plane spatial encoding in MRI and its central role in determining contrast and artifact with RF echo planar techniques. Concepts Magn. Reson. **4:** 307–325
7 Hennig J., Nauerth A. and Friedburg H. (1986) RARE imaging: a fast imaging method for clinical MR. Magn. Reson. Med. **3:** 823–833
8 Mulkern R. V., Wong S. T., Winalski C. and Jolesz F. A. (1990) Contrast manipulation and artifact assessment of 2D and 3D RARE sequences. Magn. Reson. Imaging **8:** 557–566
9 Melki P. S., Mulkern R. V., Panych L. P. and Jolesz F. A. (1991) Comparing the FAISE method with conventional dual-echo sequences. J. Magn. Reson. Imaging **1:** 319–326
10 Melki P. S., Jolesz F. A. and Mulkern R. V. (1992) Partial RF echo planar imaging with the FAISE method. I. Experimental and theoretical assessment of artifact. Magn. Reson. Med. **26:** 328–341
11 Melki P. S., Jolesz F. A. and Mulkern R. V. (1992) Partial RF echo-planar imaging with the FAISE method. II. Contrast equivalence with spin-echo sequences. Magn. Reson. Med **26:** 342–354
12 Henkelman R. M., Hardy P. A., Bishop J. E., Poon C. S. and Plewes D. B. (1992) Why fat is bright in RARE and fast spin-echo imaging. J. Magn. Reson. Imaging **2:** 533–540
13 Williamson D. S., Mulken R. V., Jakab P. D. and Jolesz F. A. (1996) Coherence transfer by isotropic mixing in Carr-Purcell-Meiboom-Gill imaging: implications for the bright fat phenomenon in fast spin-echo imaging. Magn. Reson. Med. **35:** 506–513
14 Traber F., Block W., Lamerichs R., Gieseke J. and Schild H. H. (2004) 1H metabolite relaxation times at 3.0 tesla: measurements of T1 and T2 values in normal brain and determination of regional differences in transverse relaxation. J Magn. Reson. Imaging **19:** 537–545

15 Wansapura J. P., Holland S. K., Dunn R. S. and Ball W. S. Jr (1999) NMR relaxation times in the human brain at 3.0 tesla. J. Magn. Reson. Imaging **9:** 531–538
16 Mlynarik V., Gruber S. and Moser E. (2001) Proton T (1) and T (2) relaxation times of human brain metabolites at 3 Tesla. NMR Biomed. **14:** 325–331
17 Posse S., Cuenod C. A., Risinger R., Le Bihan D. and Balaban R. S. (1995) Anomalous transverse relaxation in 1H spectroscopy in human brain at 4 Tesla. Magn. Reson. Med. **33:** 246–252
18 Rybicki F. J., Mulkern R. V., Robertson R. L., Robson C. D., Chung T. and Ma J. (2001) Fast three-point Dixon MR imaging of the retrobulbar space with low-resolution images for phase correction: comparison with fast spin-echo inversion recovery imaging. AJNR Am. J. Neuroradiol. **22:** 1798–1802
19 Le Bihan D., Mangin J. F., Poupon C., Clark C. A., Pappata S., Molko N. et al. (2001) Diffusion tensor imaging: concepts and applications. J. Magn. Reson. Imaging **13:** 534–546
20 Callaghan P. T. (1991) Principles of Nuclear Magnetic Resonance Microscopy, Oxford, Clarendon
21 Stejskal E. O. and Tanner J. E. (1965) Spin diffusion measurements: spin echos in the presence of a time-dependent field gradient. J. Chem. Phys. **42:** 288–292
22 Le Bihan D., Breton E., Lallemand D., Grenier P., Cabanis E. and Laval-Jeantet M. (1986) MR imaging of intravoxel incoherent motions: application to diffusion and perfusion in neurologic disorders. Radiology **161:** 401–407
23 Turner R. and Le Bihan D. (1990) Single-shot diffusion imaging at 2.0 Tesla. J. Magn. Reson. **86:** 445–452
24 Beaulieu C. (2002) The basis of anisotropic water diffusion in the nervous system – a technical review. NMR Biomed. **15:** 435–455
25 Takahashi M., Ono J., Harada K., Maeda M. and Hackney D. B. (2000) Diffusional anisotropy in cranial nerves with maturation: quantitative evaluation with diffusion MR imaging in rats. Radiology **216:** 881–885
26 Basser P. J., Pajevic S., Pierpaoli C., Duda J. and Aldroubi A. (2000) *In vivo* fiber tractography using DT-MRI data. Magn. Reson. Med. **44:** 625–632
27 Mori S., Crain B. J., Chacko V. P. and Zijl P. C. van (1999) Three-dimensional tracking of axonal projections in the brain by magnetic resonance imaging. Ann. Neurol. **45:** 265–269
28 Stieltjes B., Kaufmann W. E., Zijl P. C. van, Fredericksen K., Pearlson G. D., Solaiyappan M. et al. (2001) Diffusion tensor imaging and axonal tracking in the human brainstem. Neuroimage **14:** 723–735
29 Parker C. J., Wheeler-Kingshott C. A. and Barker G. J. (2002) Estimating distributed anatomical connectivity using fast marching methods and diffusion tensor imaging. IEEE Trans. Med. Imaging **21:** 505–512
30 Parker G. J., Stephan K. E., Barker G. J., Rowe J. B., MacManus D. G., Wheeler-Kingshott C. A. et al. (2002) Initial demonstration of *in vivo* tracing of axonal projections in the macaque brain and comparison with the human brain using diffusion tensor imaging and fast marching tractography. Neuroimage **15:** 797–809
31 Parker G. J., Haroon H. A. and Wheeler-Kingshott C. A. (2003) A framework for a streamline-based probabilistic index of connectivity (PICo) using a structural interpretation of MRI diffusion measurements. J. Magn. Reson. Imaging **18:** 242–254
32 Ciccarelli O., Parker G. J., Toosy A. T., Wheeler-Kingshott C. A., Barker G. J., Boulby P. A. et al. (2003) From diffusion tractography to quantitative white matter tract measures: a reproducibility study. Neuroimage **18:** 348–359
33 Chenevert T. L., Brunberg J. A. and Pipe J. G. (1990) Anisotropic diffusion in human white matter: demonstration with MR techniques *in vivo*. Radiology **177:** 401–405
34 Moseley M. E., Cohen Y., Kucharczyk J., Mintorovitch J., Asgari H. S., Wendland M. F. et al. (1990) Diffusion-weighted MR imaging of anisotropic water diffusion in cat central nervous system. Radiology **176:** 439–445
35 Basser P. J., Mattiello J. and LeBihan D. (1994) MR diffusion tensor spectroscopy and imaging. Biophys. J. **66:** 259–267
36 Pierpaoli C. and Basser P.J (1996) Toward a quantitative assessment of diffusion anisotropy. Magn. Reson. Med. **36:** 893–906
37 Pierpaoli C., Jezzard P., Basser P. J., Barnett A. and Di Chiro G. (1996) Diffusion tensor MR imaging of the human brain. Radiology **201:** 637–648
38 Basser P. J. and Pierpaoli C. (1998) A simplified method to measure the diffusion tensor from seven MR images. Magn. Reson. Med. **39:** 928–934
39 Gonzalez R. G., Schaefer P. W., Buonanno F. S., Schwamm L. H., Budzik R. F., Rordorf G. et al. (1999) Diffusion-weighted MR imaging: diagnostic accuracy in patients imaged within 6 ours of stroke symptom onset. Radiology **210:** 155–162
40 Schaefer P. W., Grant P. E. and Gonzalez R. G. (2000) Diffusion-weighted MR imaging of the brain. Radiology **217:** 331–345
41 Schlaug G., Benfield A., Baird A. E., Siewert B., Lovblad K. O., Parker R. A. et al. (1999) The ischemic penumbra: operationally defined by diffusion and perfusion MRI Neurol. **3:** 1528–1537
42 Neil J. J., Shiran S. I., McKinstry R. C., Schefft G. L., Snyder A. Z., Almli C. R. et al. (1998) Normal brain in human newborns: apparent diffusion coefficient and diffusion anisotropy measured by using diffusion tensor MR imaging. Radiology **209:** 57–66
43 Huppi P. S., Maier S. E., Peled S., Zientara G. P., Barnes P. D., Jolesz F. A. et al. (1998) Microstructural development of human newborn cerebral white matter assessed *in vivo* by diffusion tensor magnetic resonance imaging. Pediatr. Res. **44:** 584–590
44 Douek P., Turner R., Pekar J., Patronas N. and Le Bihan D. (1991) MR color mapping of myelin fiber orientation. J. Comput. Assist. Tomogr. **15:** 923–929
45 Pajevic S. and Pierpaoli C. (1999) Color schemes to represent the orientation of anisotropic tissues from diffusion tensor data: application to white matter fiber tract mapping in the human brain. Magn. Reson. Med. **42:** 526–540
46 Makris N., Worth A. J., Sorensen A. G., Papadimitriou G. M., Wu O., Reese T. G. et al. (1997) Morphometry of *in vivo* human white matter association pathways with diffusion-weighted magnetic resonance imaging. Ann. Neurol. **42:** 951–962
47 Conturo T. E., Lori N. F., Cull T. S., Akbudak, E, Snyder, A. Z., Shimony J. S. et al. (1999) Tracking neuronal fiber pathways in the living human brain. Proc. Natl. Acad. Sci. USA **96:** 10422–10427
48 Song S. K., Sun S. W., Ramsbottom M. J., Chang C., Russell J. and Cross A. H. (2002) Dysmyelination revealed through MRI as increased radial (but unchanged axial) diffusion of water. Neuroimage **17:** 1429–1436
49 Witwer B. P., Moftakhar R., Hasan K. M., Deshmukh P., Haughton V., Field A. et al. (2002) Diffusion-tensor imaging of white matter tracts in patients with cerebral neoplasm. J. Neurosurg. **97:** 568–575
50 Talos I. F., O'Donnell L., Westin C. F., Warfield S. K., Wells W. IIIrd, Yoo S. S. et al. (2003) Diffusion tensor and functional MRI fusion with anatomical MRI for image-guided neurosurgery. Lecture Notes Comput. Sci. **2878:** 407–415
51 Wolf G. L. and Fobben E. S. (1984) The tissue proton T1 and T2 response to gadolinium DTPA injection in rabbits: a potential renal contrast agent for NMR imaging. Invest. Radiol. **19:** 324–328

52 Edelman R. R., Mattle H. P., Atkinson D. J., Hill T., Finn J. P., Mayman C. et al. (1990) Cerebral blood flow: assessment with dynamic contrast-enhanced T2*-weighted MR imaging at 1.5 T. Radiology **176:** 211–220

53 Ostergaard L., Sorensen A. G., Kwong K. K., Weisskoff R. M., Gyldensted C. and Rosen B. R. (1996) High resolution measurement of cerebral blood flow using intravascular tracer bolus passages. II. Experimental comparison and preliminary results. Magn. Reson. Med. **36:** 726–736

54 Ostergaard L., Weisskoff R. M., Chesler D. A., Gyldensted C. and Rosen B. R. (1996) High resolution measurement of cerebral blood flow using intravascular tracer bolus passages. I. Mathematical approach and statistical analysis. Magn. Reson. Med. **36:** 715–725

55 Wang J., Zhang Y., Wolf R. L., Roc A. C., Alsop D. C. and Detre J. A. (2005) Amplitude-modulated continuous arterial spin-labeling 3.0-T perfusion MR imaging with a single coil: feasibility study. Radiology **235:** 218–228

56 Detre J. A., Leigh J. S., Williams D. S. and Koretsky A. P. (1992) Perfusion imaging. Magn. Reson. Med. **23:** 37–45

57 Kim S. G. (1995) Quantification of relative cerebral blood flow change by flow-sensitive alternating inversion recovery (FAIR) technique: application to functional mapping. Magn. Reson. Med. **34:** 293–301

58 Wolf R. L., Alsop D. C., McGarvey M. L., Maldjian J. A., Wang J. and Detre J. A. (2003) Susceptibility contrast and arterial spin labeled perfusion MRI in cerebrovascular disease. J. Neuroimaging **13:** 17–27

59 Garcia D. M., Duhamel G. and Alsop D. C. (2005) Efficiency of inversion pulses for background suppressed arterial spin labeling. Magn. Reson. Med. **54:** 366–372

60 Logothetis N. K., Pauls J., Augath M., Trinath T. and Oeltermann A. (2001) Neurophysiological investigation of the basis of the fMRI signal. Nature **412:** 150–157

61 Speck O., Ernst T. and Chang L. (2001) Biexponential modeling of multigradient-echo MRI data of the brain. Magn. Reson. Med. **45:** 1116–1121

62 Rivkin M. J., Wolraich D., Als H., McAnulty G., Butler S., Conneman N. et al. (2004) Prolonged T*2 values in newborn versus adult brain: implications for fMRI studies of newborns. Magn. Reson. Med. **51:** 1287–1291

63 Friston K. J., Holmes A. P., Poline J. B., Grasby P. J., Williams S. C., Frackowiak R. S. et al. (1995) Analysis of fMRI time-series revisited. Neuroimage **2:** 45–53

64 Josephs O. and Henson R. N. (1999) Event-related functional magnetic resonance imaging: modelling, inference and optimization. Phil. Trans. R. Soc. Lond. B. Biol. Sci. **354:** 1215–1228

65 Dale A. M. and Buckner R. L. (1997) Selective averaging of rapidly presented individual trials using fMRI. Hum. Brain Map. **5:** 329–340

66 Ogawa S., Tank D. W., Menon R., Ellermann J. M., Kim S. G., Merkle H. et al. (1992) Intrinsic signal changes accompanying sensory stimulation: functional brain mapping with magnetic resonance imaging. Proc. Natl. Acad. Sci. USA **89:** 5951–5955

67 Kwong K. K., Belliveau J. W., Chesler D. A., Goldberg I. E., Weisskoff R. M., Poncelet B. P. et al. (1992) Dynamic magnetic resonance imaging of human brain activity during primary sensory stimulation. Proc. Natl. Acad. Sci. USA **89:** 5675–5679

68 Constable R. T., McCarthy G., Allison T., Anderson A. W. and Gore J. C. (1993) Functional brain imaging at 1.5 T using conventional gradient echo MR imaging techniques. Magn. Reson. Imaging **11:** 451–459

69 Stroman P. W., Kornelsen J., Lawrence J. and Malisza K. L. (2005) Functional magnetic resonance imaging based on SEEP contrast: response function and anatomical specificity. Magn. Reson. Imaging **23:** 843–850

70 Oja J. M., Gillen J., Kauppinen R. A., Kraut M. and Zijl P. C. van (1999) Venous blood effects in spin-echo fMRI of human brain. Magn. Reson. Med. 42(4): 617–626

71 Song A. W., Mao H., Muthupillai R., Haist F. and Dixon W. T. (1999) Segmented spin-echo pulses to increase fMRI signal: repeated intrinsic diffusional enhancement. Magn. Reson. Med. **42:** 631–635

72 Song A. W. and Li T. (2003) Improved spatial localization based on flow-moment-nulled and intra-voxel incoherent motion-weighted fMRI. NMR Biomed. **16:** 137–143

73 Miller B. L. (1991) A review of chemical issues in 1H NMR spectroscopy: N-acetyl-L-aspartate, creatine and choline. NMR Biomed. **4:** 47–52

74 Govindaraju V., Young K. and Maudsley A. A. (2000) Proton NMR chemical shifts and coupling constants for brain metabolites. NMR Biomed. **13:** 129–153

75 Birken D. L. and Oldendorf W. H. (1989) N-acetyl-L-aspartic acid: a literature review of a compound prominent in 1H-NMR spectroscopic studies of brain. Neurosci. Biobehav. Rev. **13:** 23–31

76 Young I. R. and Charles H. C. (1996) MR spectroscopy: Clinical Applications and Techniques, pp. 27–40, Dunitz, London

77 Abragam A. (1962) Principles of Nuclear Magnetism, pp. 159–215, 480–510, Clarendon, Oxford

78 Bottomley P. A. (1987) Spatial localization in NMR spectroscopy *in vivo*. Ann. NY Acad. Sci. **508:** 333–348

79 Frahm J., Merboldt K. D. and Hanicke W. (1987) Localized spectroscopy using stimulated echoes. J. Magn. Reson. **72:** 502–508

80 Brown T. R., Kincaid B. M. and Ugurbil K. (1982) NMR chemical shift imaging in three dimensions. Proc. Natl. Acad. Sci. USA **79:** 3523–3526

81 Mulkern R. V., Chen N. K., Oshio K., Panych L. P., Rybicki F. J. and Gambarota G. (2004) Fast spectroscopic imaging strategies for potential applications in fMRI. Magn. Reson. Imaging **22:** 1395–1405

82 Dydak U., Weiger M., Pruessmann K. P., Meier D. and Boesiger P (2001) Sensitivity-encoded spectroscopic imaging. Magn. Reson. Med. **46:** 713–722

83 Simmons M. L., Frondoza C. G. and Coyle J. T. (1991) Immunocytochemical localization of N-acetyl-aspartate with monoclonal antibodies. Neuroscience **45:** 37–45

84 Urenjak J., Williams S. R., Gadian D. G. and Noble M. (1992) Specific expression of N-acetylaspartate in neurons, oligodendrocyte-type-2 astrocyte progenitors, and immature oligodendrocytes *in vitro*. J. Neurochem. **59:** 55–61

85 Bhakoo K. K. and Pearce D. (2000) *In vitro* expression of N-acetyl aspartate by oligodendrocytes: implications for proton magnetic resonance spectroscopy signal *in vivo*. J. Neurochem. **74:** 254–262

86 De Stefano N., Matthews P. M. and Arnold D. L. (1995) Reversible decreases in N-acetylaspartate after acute brain injury. Magn. Reson. Med. **34:** 721–727

87 Toft P. B., Christiansen P., Pryds O., Lou H. C. and Henriksen O. (1994) T1, T2, and concentrations of brain metabolites in neonates and adolescents estimated with H-1 MR spectroscopy. J. Magn. Reson. Imaging **4:** 1–5

88 Kok R. D., Berg P. P. van den, Bergh A. J. van den, Nijland R. and Heerschap A. (2002) Maturation of the human fetal brain as observed by 1H MR spectroscopy. Magn. Reson. Med. **48:** 611–616

89 Preul M. C., Caramanos Z, Collins D. L., Villemure J. G., Leblanc R., Olivier A. et al. (1996) Accurate, noninvasive diagnosis of human brain tumors by using proton magnetic resonance spectroscopy. Nat. Med. **2:** 323–325

90 Herminghaus S., Dierks T., Pilatus U., Moller-Hartmann W., Wittsack J., Marquardt G. et al. (2003) Determination of histopathological tumor grade in neuroepithelial brain tumors by

using spectral pattern analysis of *in vivo* spectroscopic data. J. Neurosurg. **98:** 74–81
91 Magalhaes A., Godfrey W., Shen Y., Hu J. and Smith W. (2005) Proton magnetic resonance spectroscopy of brain tumors correlated with pathology. Acad. Radiol. **12:** 51–57
92 Kreis R., Ernst T. and Ross B. D. (1993) Development of the human brain: *in vivo* quantification of metabolite and water content with proton magnetic resonance spectroscopy. Magn. Reson. Med. **30:** 424–437
93 Saunders D. E., Howe F. A., Boogaart A. van den, Griffiths J. R. and Brown M. M. (1999) Aging of the adult human brain: *in vivo* quantitation of metabolite content with proton magnetic resonance spectroscopy. J. Magn. Reson. Imaging **9:** 711–716
94 Lim K. O. and Spielman D. M. (1997) Estimating NAA in cortical gray matter with applications for measuring changes due to aging. Magn. Reson. Med. **37:** 372–377
95 Lundbom N., Barnett A., Bonavita, S, Patronas, N, Rajapakse J. and Tedeschi G. (1999) MR image segmentation and tissue metabolite contrast in 1H spectroscopic imaging of normal and aging brain. Magn. Reson. Med. **41:** 841–845
96 Pouwels P. J. and Frahm J. (1998) Regional metabolite concentrations in human brain as determined by quantitative localized proton MRS. Magn. Reson. Med. **39:** 53–60
97 Kreis R. (1997) Quantitative localized 1H MR spectroscopy for clinical use. Prog. Magn. Reson. Spectrosc. **31:** 155–195
98 Wang Y. and Li S. J. (1998) Differentiation of metabolic concentrations between gray matter and white matter of human brain by *in vivo* 1H magnetic resonance spectroscopy. Magn. Reson. Med. **39:** 28–33
99 Michaelis T., Merboldt K. D., Bruhn H., Hanicke W. and Frahm J. (1993) Absolute concentrations of metabolites in the adult human brain *in vivo*: quantification of localized proton MR spectra. Radiology **187:** 219–227
100 Komoroski R. A., Heimberg C., Cardwell D. and Karson C. N. (1999) Effects of gender and region on proton MRS of normal human brain. Magn. Reson. Imaging **17:** 427–433
101 Noworolski S. M., Nelson S. J., Henry R. G., Day M. R., Wald L. L., Star-Lack J. et al. (1999) High spatial resolution 1H-MRSI and segmented MRI of cortical gray matter and subcortical white matter in three regions of the human brain. Magn. Reson. Med. **41:** 21–29
102 Nelson S. J., Vigneron D. B. and Dillon W. P. (1999) Serial evaluation of patients with brain tumors using volume MRI and 3D 1H MRSI. NMR Biomed. **12:** 123–138
103 Adamson A. J., Rand S. D., Prost R. W., Kim T. A., Schultz C. and Haughton V. M. (1998) Focal brain lesions: effect of single-voxel proton MR spectroscopic findings on treatment decisions. Radiology **209:** 73–78
104 Chan Y. L., Yeung D. K., Leung S. F. and Cao G. (1999) Proton magnetic resonance spectroscopy of late delayed radiation-induced injury of the brain. J. Magn. Reson. Imaging **10:** 130–137
105 Taylor J. S., Langston J. W., Reddick W. E., Kingsley P. B., Ogg R. J., Pui M. H. et al. (1996) Clinical value of proton magnetic resonance spectroscopy for differentiating recurrent or residual brain tumor from delayed cerebral necrosis. Int. J. Radiat. Oncol. Biol. Phys. **36:** 1251–1261
106 Sijens P. E., Levendag P. C., Vecht C. J., Dijk P. van and Oudkerk M. (1996) 1H MR spectroscopy detection of lipids and lactate in metastatic brain tumors. NMR Biomed. **9:** 65–71
107 Tsai G. and Coyle J. T. (1995) N-acetylaspartate in neuropsychiatric disorders. Prog. Neurobiol. **46:** 531–540
108 Davies S. E., Newcombe J., Williams S. R., McDonald W. I. and Clark J. B. (1995) High resolution proton NMR spectroscopy of multiple sclerosis lesions. J. Neurochem. **64:** 742–748
109 Shonk T. K., Moats R. A., Gifford P., Michaelis T., Mandigo J. C., Izumi J. et al. (1995) Probable Alzheimer disease: diagnosis with proton MR spectroscopy. Radiology **195:** 65–72
110 Moats R. A., Ernst T., Shonk T. K. and Ross B. D. (1994) Abnormal cerebral metabolite concentrations in patients with probable Alzheimer disease. Magn. Reson. Med. **32:** 110–115
111 Doraiswamy P. M., Charles H. C. and Krishnan K. R. (1998) Prediction of cognitive decline in early Alzheimer's disease. Lancet **352:** 1678
112 Provencher S. W. (1993) Estimation of metabolite concentrations from localized *in vivo* proton NMR spectra. Magn. Reson. Med. **30:** 672–679
113 Young K., Govindaraju V., Soher B. J. and Maudsley A. A. (1998) Automated spectral analysis. I. Formation of a priori information by spectral simulation. Magn. Reson. Med. **40:** 812–815
114 Stoll A. L., Renshaw P. F., De Micheli E., Wurtman R., Pillay S. S. and Cohen B. M. (1995) Choline ingestion increases the resonance of choline-containing compounds in human brain: an *in vivo* proton magnetic resonance study. Biol. Psychiatry **37:** 170–174
115 Tan J., Bluml S., Hoang T., Dubowitz D., Mevenkamp G. and Ross B. (1998) Lack of effect of oral choline supplement on the concentrations of choline metabolites in human brain. Magn. Reson. Med. **39:** 1005–1010
116 Meyerhoff D. J., Rooney W. D., Tokumitsu T. and Weiner M. W. (1996) Evidence of multiple ethanol pools in the brain: an *in vivo* proton magnetization transfer study. Alcohol Clin. Exp. Res. **20:** 1283–1288
117 Kaufman M. J., Chiu T. M., Mendelson J. H., Woods B. T., Teoh S. K., Eros-Sarnyai M. et al. (1996) Brain alcohol detectability increase with repeated administration in humans: a proton spectroscopy study. Magn. Reson. Med. **35:** 435–440
118 Serafini S., Steury K., Richards T., Corina D., Abbott R., Dager S. R. et al. (2001) Comparison of fMRI and PEPSI during language processing in children. Magn. Reson. Med. **45:** 217–225
119 Urrila A. S., Hakkarainen A., Heikkinen S., Vuori K., Stenberg D., Hakkinen A. M. et al. (2003) Metabolic imaging of human cognition: an fMRI/1H-MRS study of brain lactate response to silent word generation. J. Cereb. Blood Flow Metab. **23:** 942–948
120 Mangia S., Garreffa G., Bianciardi M., Giove F., Di Salle F. and Maraviglia B. (2003) The aerobic brain: lactate decrease at the onset of neural activity. Neuroscience **118:** 7–10
121 Prichard J., Rothman D., Novotny E., Petroff O., Kuwabara T., Avison M. et al. (1991) Lactate rise detected by 1H NMR in human visual cortex during physiologic stimulation. Proc. Natl. Acad. Sci. USA **88:** 5829–5831
122 Sappey-Marinier D., Calabrese G., Fein G., Hugg J. W., Biggins C. and Weiner M. W. (1992) Effect of photic stimulation on human visual cortex lactate and phosphates using 1H and 31P magnetic resonance spectroscopy. J. Cereb. Blood Flow Metab. **12:** 584–592
123 Lee H. K., Yaman A. and Nalcioglu O. (1995) Homonuclear J-refocused spectral editing technique for quantification of glutamine and glutamate by 1H NMR spectroscopy. Magn. Reson. Med. **34:** 253–259
124 Bielicki G., Chassain C., Renou J. P., Farges M. C., Vasson M. P., Eschalier A. et al. (2004) Brain GABA editing by localized *in vivo* (1)H magnetic resonance spectroscopy. NMR Biomed. **17:** 60–68
125 Jensen J. E., Frederick B. D., Wang L., Brown J. and Renshaw P. F. (2005) Two-dimensional, J-resolved spectroscopic imaging of GABA at 4 Tesla in the human brain. Magn. Reson. Med. **54:** 783–788
126 Allen P. S., Thompson R. B. and Wilman A. H. (1997) Metabolite-specific NMR spectroscopy *in vivo*. NMR Biomed. **10:** 435–444
127 Hardy D. L. and Norwood T. J. (1998) Spectral editing technique for the *in vitro* and *in vivo* detection of taurine. J. Magn. Reson. **133:** 70–78

128 Pan J. W., Mason G. F., Pohost G. M. and Hetherington H. P. (1996) Spectroscopic imaging of human brain glutamate by water-suppressed J-refocused coherence transfer at 4.1 T. Magn. Reson. Med. **36:** 7–12
129 Thompson R. B. and Allen P. S. (1998) A new multiple quantum filter design procedure for use on strongly coupled spin systems found *in vivo*: its application to glutamate. Magn. Reson. Med. **39:** 762–771
130 Du F., Chu W. J., Yang B., Den Hollander J. A. and Ng T. C. (2004) *In vivo* GABA detection with improved selectivity and sensitivity by localized double quantum filter technique at 4.1T. Magn. Reson. Imaging **22:** 103–108
131 Choi I. Y., Lee S. P., Merkle H. and Shen J. (2004) Single-shot two-echo technique for simultaneous measurement of GABA and creatine in the human brain *in vivo*. Magn. Reson. Med. **51:** 1115–1121
132 Provencher S. W. (2001) Automatic quantitation of localized *in vivo* 1H spectra with LCModel. NMR Biomed. **14:** 260–264
133 Pfeuffer J., Tkac I., Provencher S. W. and Gruetter R. (1999) Toward an *in vivo* neurochemical profile: quantification of 18 metabolites in short-echo-time (1)H NMR spectra of the rat brain. J. Magn. Reson. **141:** 104–120
134 Ross B. and Bluml S. (2001) Magnetic resonance spectroscopy of the human brain. Anat. Rec. **265:** 54–84
135 Hetherington H. P., Spencer D. D., Vaughan J. T. and Pan J. W. (2001) Quantitative (31)P spectroscopic imaging of human brain at 4 Tesla: assessment of gray and white matter differences of phosphocreatine and ATP. Magn. Reson. Med. **45:** 46–52
136 Arias-Mendoza F. (2004) *In vivo* magnetic resonance spectroscopy in the evaluation of mitochondrial disorders. Mitochondrion **4:** 491–501
137 Theberge J., Al-Semaan Y., Jensen J. E., Williamson P. C., Neufeld R. W., Menon R. S. et al. (2004) Comparative study of proton and phosphorus magnetic resonance spectroscopy in schizophrenia at 4 Tesla. Psychiatry Res. **132:** 33–39
138 Bischof M. G., Mlynarik V., Brehm A., Bernroider E., Krssak M., Bauer E. et al. (2004) Brain energy metabolism during hypoglycaemia in healthy and type 1 diabetic subjects. Diabetologia **47:** 648–651
139 Maintz D., Heindel W., Kugel H., Jaeger R. and Lackner K. J. (2002) Phosphorus-31 MR spectroscopy of normal adult human brain and brain tumours. NMR Biomed. **15:** 18–27
140 Cady E. B. (2001) Magnetic resonance spectroscopy in neonatal hypoxic-ischaemic insults. Childs Nerv. Syst. **17:** 145–149
141 Gruetter R., Novotny E. J., Boulware S. D., Mason G. F., Rothman D. L., Shulman G. I. et al. (1994) Localized 13C NMR spectroscopy in the human brain of amino acid labeling from D-[1–13C]glucose. J. Neurochem. **63:** 1377–1385
142 Gruetter R., Novotny E. J., Boulware S. D., Rothman D. L., Mason G. F., Shulman G. I. et al. (1992) Direct measurement of brain glucose concentrations in humans by 13C NMR spectroscopy. Proc. Natl. Acad. Sci. USA **89:** 1109–1112
143 Bluml S. (1999) *In vivo* quantitation of cerebral metabolite concentrations using natural abundance 13C MRS at 1.5 T. J. Magn. Reson. **136:** 219–225
144 Gruetter R., Seaquist E. R., Kim S. and Ugurbil K. (1998) Localized *in vivo* 13C-NMR of glutamate metabolism in the human brain: initial results at 4 tesla. Dev. Neurosci. **20:** 380–388
145 Bluml S., Moreno A., Hwang J. H. and Ross B. D. (2001) 1-(13)C glucose magnetic resonance spectroscopy of pediatric and adult brain disorders. NMR Biomed. **14:** 19–32
146 Berendsen H. J. and Edzes H. T. (1973) The observation and general interpretation of sodium magnetic resonance in biological material. Ann. NY Acad. Sci. **204:** 459–485
147 Maudsley A. A. and Hilal S. K. (1984) Biological aspects of sodium-23 imaging. Br. Med. Bull. **40:** 165–166
148 Winkler S. S., Thomasson D. M., Sherwood K. and Perman W. H. (1989) Regional T2 and sodium concentration estimates in the normal human brain by sodium-23 MR imaging at 1.5 T. J. Comput. Assist. Tomogr. **13:** 561–566
149 Boada F. E., Gillen J. S., Shen G. X., Chang S. Y. and Thulborn K. R. (1997) Fast three dimensional sodium imaging. Magn. Reson. Med. **37:** 706–715
150 Clayton D. B. and Lenkinski R. E. (2003) MR imaging of sodium in the human brain with a fast three-dimensional gradient-recalled-echo sequence at 4 T. Acad. Radiol. **10:** 358–365